The Astrophysical Journal Letters, 890:L14 (8pp), 2020 February 10 https://doi.org/10.3847/2041-8213/ab70b8

Shaping the Envelope of the Asymptotic Giant Branch Star W43A with a Collimated Fast Jet

Daniel Tafoya[1,2], Hiroshi Imai[3,4], José F. Gómez[5], Jun-ichi Nakashima[6], Gabor Orosz[7,8], and Bosco H. K. Yung[9]
[1] Department of Space, Earth and Environment, Chalmers University of Technology, Onsala Space Observatory, SE-439 92 Onsala, Sweden
daniel.tafoya@chalmers.se
[2] Chile Observatory, National Astronomical Observatory of Japan, National Institutes of Natural Sciences, 2-21-1 Osawa, Mitaka, Tokyo 181-8588, Japan
[3] Center for General Education, Institute for Comprehensive Education, Kagoshima University, 1-21-30 Korimoto, Kagoshima 890-0065, Japan
[4] Amanogawa Galaxy Astronomy Research Center, Graduate School of Science and Engineering, Kagoshima University, 1-21-35 Korimoto, Kagoshima 890-0065, Japan
[5] Instituto de Astrofísica de Andalucía, CSIC, Glorieta de la Astronomía s/n, E-18008 Granada, Spain
[6] Department of Astronomy, School of Physics and Astronomy, Sun Yat-sen University, Zhuhai 519082, People's Republic of China
[7] School of Natural Sciences, University of Tasmania, Private Bag 37, Hobart, Tasmania 7001, Australia
[8] Xinjiang Astronomical Observatory, Chinese Academy of Sciences, 150 Science 1-Street, Urumqi, Xinjiang 830011, People's Republic of China
[9] Nicolaus Copernicus Astronomical Center, Rabiańska 8, 87-100 Toruń, Poland
Received 2020 January 20; revised 2020 January 24; accepted 2020 January 28; published 2020 February 13

Abstract

One of the major puzzles in the study of stellar evolution is the formation process of bipolar and multipolar planetary nebulae. There is growing consensus that collimated jets create cavities with dense walls in the slowly expanding (10–20 km s^{-1}) envelope ejected in previous evolutionary phases, leading to the observed morphologies. However, the launching of the jet and the way it interacts with the circumstellar material to create such asymmetric morphologies have remained poorly known. Here we present for the first time CO emission from the asymptotic giant branch star W43A that traces the whole stream of a jet, from the vicinity of its driving stellar system out to the regions where it shapes the circumstellar envelope. We found that the jet has a launch velocity of 175 km s^{-1} and decelerates to a velocity of 130 km s^{-1} as it interacts with circumstellar material. The continuum emission reveals a bipolar shell with a compact bright dot in the center that pinpoints the location of the driving source of the jet. The kinematical ages of the jet and the bipolar shell are equal, $\tau \sim 60$ yr, indicating that they were created simultaneously, probably by a common underlying mechanism, and in an extremely short time. These results provide key initial conditions for the theoretical models that aim to explain the formation of bipolar morphologies in the circumstellar envelopes of low- and intermediate-mass stars.

Unified Astronomy Thesaurus concepts: Asymptotic giant branch stars (2100); Stellar jets (1607)

1. Introduction

In the past couple of decades there has been mounting observational evidence that, after the asymptotic giant branch (AGB) phase, low- and intermediate-mass ($M \lesssim 8M_{\odot}$) stars develop powerful highly collimated outflows that have a strong impact on the circumstellar envelope (CSE) that forms in previous mass-loss episodes. One important effect of the activity of such collimated outflows is sculpting and modifying the shape of the roughly spherical CSE (e.g., Sahai & Trauger 1998). According to the increasingly popular model proposed by Sahai & Trauger (1998) to explain the formation of asymmetric planetary nebulae, the fast collimated outflows carve cavities within the spherical CSE that are eventually seen as bright lobes and bubble-like morphologies in the subsequent planetary nebula phase, when the star becomes hot enough to ionize the CSE. This process occurs in a very short timescale ($\lesssim$1000 yr), during which the star becomes enshrouded by gas and dust that render it invisible at optical wavelengths. As a result, it is difficult to find objects undergoing this ephemeral phase. Nonetheless, there is a particular group, containing 15 known sources in our Galaxy, of oxygen-rich post-AGB objects that exhibit high-velocity H_2O masers ($v_{exp} \gtrsim 100$ km s^{-1}) tracing collimated structures and/or bow shocks (Imai 2007). These objects are called water fountains (WFs) and they are thought to be undergoing the earliest manifestation of collimated mass loss after the AGB phase (Likkel & Morris 1988). Thus, the study of WFs is of great importance to understand the evolution of low- and intermediate-mass stars since they hold key information to understand the launching and collimation of jets in the late phases of these sources, as well as their interaction with the CSE.

W43A, located at a distance of 2.2 kpc from the Sun (see Appendix A), is surrounded by a thick dusty envelope that renders it invisible at optical and near-infrared (IR) wavelengths (Wilson & Barrett 1972). The mid-IR images reveal an elongated structure (1.″2 × 1.″6) oriented along a position angle (PA) ∼62° (Lagadec et al. 2011). The presence of hydroxyl (OH) masers with a periodic variability and the silicon monoxide (SiO) maser emission strongly suggest that W43A hosts an AGB star (Herman & Habing 1985; Imai et al. 2005). Furthermore, the bipolar distribution of the SiO masers and the discovery of highly collimated water (H_2O) maser structures indicate that this source is undergoing the ephemeral transition in which the spherical CSE formed during the AGB phase develops a bipolar morphology (Diamond & Nyman 1988; Imai et al. 2002, 2005; Vlemmings et al. 2006; Amiri et al. 2010; Chong et al. 2015). The H_2O masers exhibit expansion velocities ($V_{H_2O} \sim 150$ km s^{-1}) much higher than that of the 1612 MHz OH masers ($V_{OH1612} \sim 8$ km s^{-1}), which gives W43A the classification of a WF source (Likkel & Morris 1988; Imai et al. 2002). The H_2O masers were originally found to be located mainly in two linear structures separated by 0.″6 on the plane of the sky, which corresponds to a deprojected separation of 1600 au considering an inclination angle with respect to the plane of the sky of 35° (Imai et al. 2002; Chong et al. 2015). The highly collimated motions and distribution of the H_2O masers suggested the presence of a jet with a kinematical age of only $\tau_{H_2O} \sim 50$ yr (Imai et al. 2002, 2005). In addition, a magnetic field of $B \approx 200 \pm 75$ mG was measured via

the Zeeman effect of the H_2O masers (Vlemmings et al. 2006). Thus, it has been thought that the H_2O masers trace the regions where a magnetically collimated jet interacts with the CSE, creating low-density cavities that will lead to the formation of an asymmetric planetary nebula when the central star becomes hot enough to ionize the surrounding gas (Imai et al. 2002; Vlemmings et al. 2006). However, since the H_2O masers do not trace the jet in its entirety, the true extent of the jet, the collimation mechanism, as well as the way it interacts with the ambient material have remained unclear (Chong et al. 2015).

2. Observations

We used the Atacama Large Millimeter/submillimeter Array (ALMA) to observe with high angular resolution ($0\farcs040 = 90$ au) the emission from the dust and molecular gas around W43A. The observations were carried out on 2017 September 22 using 42 antennas of the ALMA 12 m array with Band 6 receivers (~230 GHz) as part of the project 2016.1.00540.S (PI: H. Imai). The maximum and minimum baseline lengths were 12.1 km and 41.4 m, respectively. The corresponding angular resolution and maximum recoverable scale are $0\farcs04$ and $0\farcs6$, respectively. The field of view of the observations was approximately $25''$. The total time of observation on W43A was 23 minutes. The data were calibrated with the ALMA pipeline using J1924−2914 (~3.4 Jy) as a flux/bandpass calibrator and J1851+0035 (~260 mJy) as a gain calibrator. Images were created with CASA 5.4.0 using a Briggs weighting scheme with the robust parameter set to 0. The continuum emission was subtracted from the data cubes, and channel maps with a spectral resolution of $\sim 1.3\,\mathrm{km\,s^{-1}}$ were created. The typical channel rms noise level is ~2 mJy beam^{-1} in line-free channels. Among the detected spectral lines, the emission of the CO($J = 2 \rightarrow 1$) and p-H_2S($J_{K_a,K_c} = 2_{20} \rightarrow 2_{11}$) lines was used for the analysis presented in this work. The continuum image was created by averaging line-free channels from three 234.375 MHz wide spectral windows giving a total bandwidth of 0.7 GHz. The central frequencies of the spectral windows used for creating the continuum are 230.282 GHz, 230.930 GHz, and 231.866 GHz, respectively. The rms level in the continuum image is ~110 μJy beam^{-1}.

3. Results and Discussion

3.1. CO Emission

The CO($J = 2 \rightarrow 1$) emission spans a total velocity range of $\sim 200\,\mathrm{km\,s^{-1}}$ and is distributed over an elongated region (deprojected size $\sim 300 \times 3500$ au) whose major axis has a PA ~ 68° (see Figure 1 and Figure 4 in Appendix B). From the channel map shown in Figure 4 in Appendix B it can be seen that the emission with the highest velocity offset,[10] $|V_{\rm offset}(\mathrm{km\,s^{-1}})| \sim 100$ (see also Figure 2), is the most collimated and lies closest to the star. For velocity offsets $75 \lesssim |V_{\rm offset}(\mathrm{km\,s^{-1}})| \lesssim 100$, the emission exhibits a high degree of collimation and it reaches locations farther away from the star than for the highest velocity offsets, i.e., it exhibits a negative velocity gradient, $|dv|/|dr| < 0$. Furthermore, for velocity offsets $0 \lesssim |V_{\rm offset}(\mathrm{km\,s^{-1}})| \lesssim 75$ the emission is less collimated and the velocity gradient inverts, i.e., the emission reaches locations farther away from the star with increasing velocity offset.

[10] The velocity offset, $V_{\rm offset}$, is defined with respect to the systemic velocity of W43A, $V_{\rm sys} = 34\,\mathrm{km\,s^{-1}}$, and corresponds to only the line-of-sight velocity component.

Thus, the CO($J = 2 \rightarrow 1$) emission can be divided into two components characterized by their spatial distributions and velocity gradient. The component with negative velocity gradient has the highest velocity offsets $75 \lesssim |V_{\rm offset}(\mathrm{km\,s^{-1}})| \lesssim 100$ and it exhibits an extremely collimated morphology all the way from the vicinity of the central star (~90 au) out to a deprojected distance of ~1600 au. The negative velocity gradient may indicate a deceleration of the emitting material as it moves away from the central system. This component is shown with gray contours in Figure 1. The other component has lower velocity offsets $0 \lesssim |V_{\rm offset}(\mathrm{km\,s^{-1}})| \lesssim 75$ and is less collimated, albeit it has a bipolar morphology and is distributed around the high-velocity component, which is shown with green contours in Figure 1. The positive velocity gradient in this component may indicate entrainment of the circumstellar material by a fast jet. The criteria to distinguish these kinematical components are further explained in Section 3.3.

3.2. Continuum Emission

The continuum emission traces a bipolar shell (color map in Figure 1; see also Figure 3) that confines parts of the low-velocity CO($J = 2 \rightarrow 1$) emission. The bipolar shell has a typical deconvolved width of 130 au and it has two bright regions that exhibit point symmetry with respect to the central source. From Figure 1 it can be seen that the CO($J = 2 \rightarrow 1$) emission is absorbed toward these bright regions, suggesting that they are optically thick regions. Therefore, the brightness temperature of the bright regions (≈110 K) is likely to be the actual temperature of the dust. Figure 1 also reveals that the bright regions lie on the sides of the shell located closest to the main axis of the jet. This may be due to the passage of the jet close to the shell causing an increase in the density and/or temperature of the dust. The average density of the shell is estimated to be $n_{\rm H_2,Shell} \approx 5 \times 10^8$ cm^{-3} (see Appendix D for the calculations), which favors the physical conditions to produce the observed H_2O masers.

There is also a bright emission source at the center of the nebula. A Gaussian fit to this source gives a deconvolved size of 90×60 au with a PA ≃ 145°, which is nearly perpendicular to the direction of the jet.

3.3. A Decelerating Collimated Jet and a Bipolar Outflow

Figure 2 shows a position–velocity (PV) diagram of the CO($J = 2 \rightarrow 1$) emission obtained with a slit along the major axis of the emitting region, PA = 68°. It is evident in this PV diagram that the spatial spread of the CO($J = 2 \rightarrow 1$) emission, delimited horizontally by the solid red and light-blue lines, increases as a function of the velocity offset for $0 \lesssim |V_{\rm offset}(\mathrm{km\,s^{-1}})| \lesssim 75$ and decreases for $75 \lesssim |V_{\rm offset}(\mathrm{km\,s^{-1}})| \lesssim 100$. Thus, this PV diagram of W43A exhibits an S-like pattern that resembles the PV diagram of the WF IRAS 16342−3814 (Sahai et al. 2011; Tafoya et al. 2019). Tafoya et al. (2019) interpreted the PV diagram of IRAS 16342−3814 in terms of a jet-driven molecular outflow where the jet decelerates as it interacts with the surrounding material, transferring kinetic energy and momentum. The surrounding material and the jet produce the emission with positive and negative gradients, respectively, in the PV diagram. Given the spatial distribution of the emission seen in Figure 1 and the profile of the PV diagram of Figure 2, it is evident that the spatio-kinematical configuration of W43A is similar to the one of IRAS 16342−3814. Following the analysis done by Tafoya et al. (2019), the launch velocity of the jet can be obtained from the

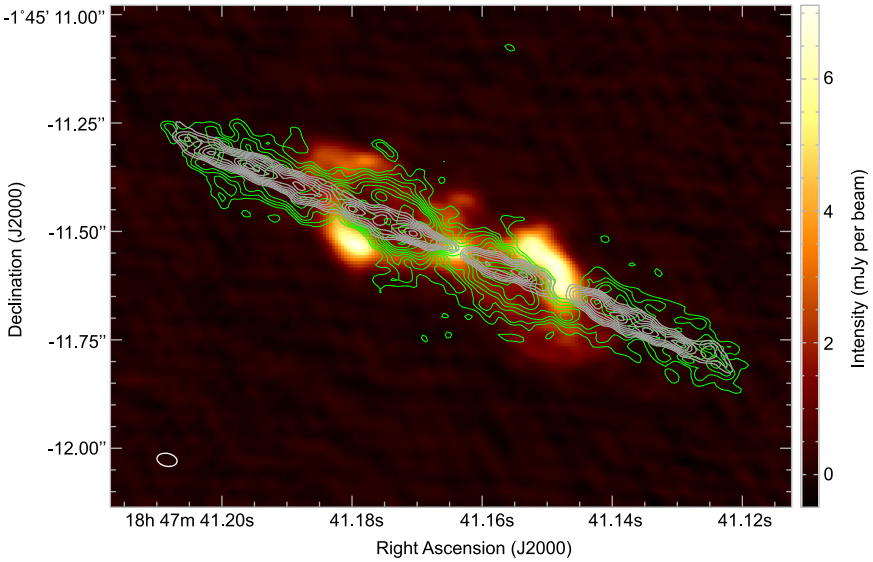

Figure 1. Continuum and CO($J = 2 \rightarrow 1$) line emission from W43A. The green contours are CO($J = 2 \rightarrow 1$) emission integrated over the range of line-of-sight velocity offset $|V_{\rm offset}\,({\rm km\,s^{-1}})| < 75$. The gray contours are CO($J = 2 \rightarrow 1$) emission integrated over the highest velocity range, $75 < |V_{\rm offset}\,({\rm km\,s^{-1}})| < 100$. The contours are drawn from 3σ on steps of 3σ ($\sigma = 15$ mJy beam^{-1} km s^{-1}). The ellipse at the bottom left corner represents the size of the synthesized beam of the CO observations, $\theta_{\rm beam} = 0\farcs048 \times 0\farcs031$, PA $= 74\fdg8$. The color map is the continuum emission at ~230 GHz and the corresponding synthesized beam is $\theta_{\rm beam} = 0\farcs047 \times 0\farcs030$, PA $= 78\fdg1$.

highest velocity offset of the CO($J = 2 \rightarrow 1$) emission, which in Figure 2 is indicated as $|V_{\rm i}| \sim 100$ km s^{-1}. Considering the inclination of the source of 35° with respect to the plane of the sky, this velocity corresponds to a deprojected expansion velocity $U_{\rm i} \equiv |V_{\rm i}|/\sin 35^\circ = 175\,{\rm km\,s^{-1}}$. The velocity offset at which the velocity gradient changes from positive to negative is $|V_{\rm offset}\,({\rm km\,s^{-1}})| \approx 75$. This value represents the velocity offset at the tip of the jet, $V_{\rm f} \approx 75\,{\rm km\,s^{-1}}$, and its corresponding deprojected expansion velocity is $U_{\rm f} \equiv |V_{\rm f}|/\sin\ 35^\circ = 130\,{\rm km\,s^{-1}}$.

This shows that the material at the tip of the jet has decelerated during its journey from the launching region to its present location. This behavior is expected if turbulent entrainment along the jet is a dominant process since, for such a case, the average velocity of the jet would decrease as momentum is transferred to the entrained material (Chernin et al. 1994). On the other hand, the overall velocity spread of the emission at a given position in the *PV* diagram, delimited vertically by the solid red and light-blue lines, decreases with the distance from central system as an effect of the lateral expansion and turbulent motion of the gas (Chernin et al. 1994; Balick et al. 2013). From Figure 2 it can be seen that beyond the radius of the outer edge of the H_2O masers clusters, $r = r_{\rm H_2O}$, the maximum velocity offset of the CO emission begins to drop significantly. Thus, it is likely that the largest deceleration occurs when the jet interacts with material of the shell, creating the physical conditions ($T \approx 400$ K; $n_{\rm H_2} \approx 10^9$ cm^{-3}) that favor H_2O maser emission (Yates et al. 1997). This would explain the high concentration of H_2O masers in the interaction region. After the jet interacts with the shell, it continues streaming outward and decelerates even further.

The collimation factor of the CO structure that traces the jet, defined as the ratio between the length and the width, is very high (~20). Surprisingly, the degree of collimation of the jet is not affected after passing the region of interaction with the bipolar shell. The persistence of the high degree of collimation of the jet after the interaction with the shell is likely due to the pressure of the magnetic field, since it is expected to dominate the gas pressure by a factor of a few hundred in the interaction region (Vlemmings et al. 2006). Even though from these observations there is no clear evidence that the jet is precessing, as opposed to what was thought from the H_2O maser observations earlier (Imai et al. 2002), it is possible that there have been some slight variations in the PA of the jet that may explain the changes seen in the distribution of the H_2O masers over the past couple of decades (Chong et al. 2015).

3.4. Timescale of the Jet and Bipolar Shell

Considering that the velocity of the jet remains roughly constant from the launching point to the H_2O maser region, the kinematical timescale for the jet to reach this location is ~30 yr. In addition, assuming that the jet suffers a constant deceleration in the region beyond the location of the H_2O masers, the kinematical timescale from the H_2O maser region to the tip of the jet is ~35 yr. Thus, the total kinematical age of the jet is of just $\tau_{\rm jet} = 65$ yr.

In addition to CO($J = 2 \rightarrow 1$), the *p*-H_2S ($J_{K_a,K_c} = 2_{20} \rightarrow 2_{11}$) line was also detected from the observations of this project. The H_2S emission is shown in Figure 5 in Appendix C superimposed on the continuum emission. As can be seen from Figure 5 in Appendix C, the H_2S emission has a spatial distribution that is significantly different from that of the CO emission. Particularly, while the later one seems to be confined by the shell in the direction perpendicular to the outflow, the former one extends beyond the shell. Figure 6 in Appendix C shows a *PV* diagram of the H_2S emission where it can be seen that it exhibits the characteristic morphology of a double-lobe structure, indicated with solid lines, similar to the morphology of the bipolar shell traced by the continuum emission. H_2S is known to trace shocked material (e.g., Holdship et al. 2016), and in the case of W43A it is most likely tracing the shock produced by the expansion of the shell. Thus, we assume that the H_2S emission traces not only the spatial distribution but also the kinematics of the bipolar shell. The kinematical age of the bipolar shell can be obtained as $\tau_{\rm shell} \approx R_{\rm shell}/V_{\rm shell}$, where $V_{\rm shell}$ is the expansion velocity of the shell at any point located at a distance $R_{\rm shell}$ from the central source. The expansion velocity of the H_2S emission at the location of the H_2O

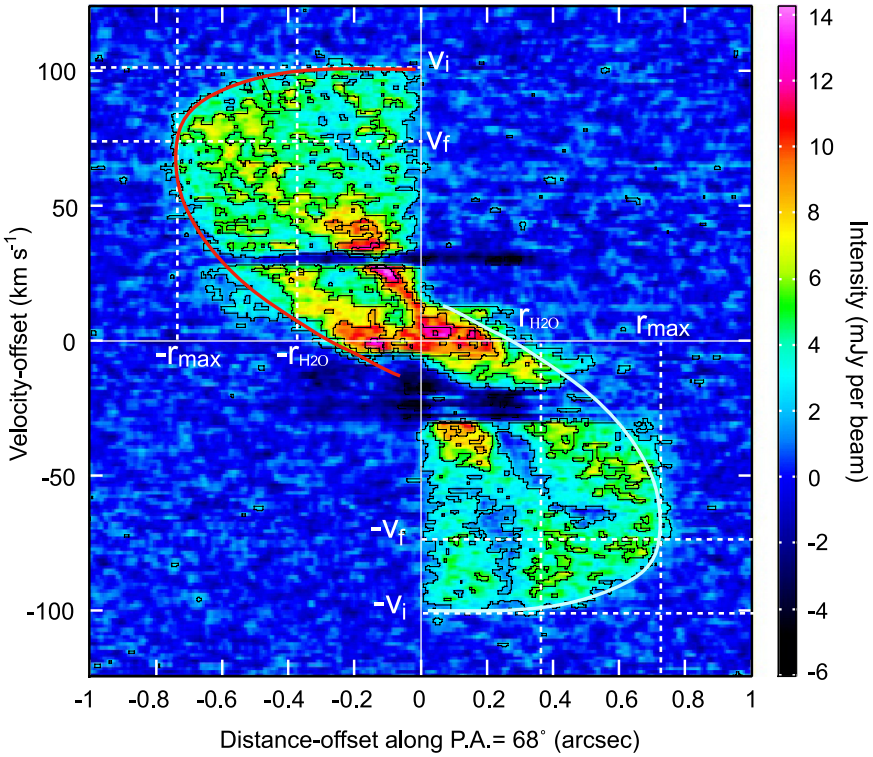

Figure 2. *PV* diagram of the CO($J = 2 \rightarrow 1$) line emission from W43A. The *PV* diagram was obtained using a slit along PA = 68°. The velocity offset is defined with respect to the systemic velocity of the star $V_{sys} = 34$ km s^{-1}. The horizontal white dashed lines indicate the maximum and minimum line-of-sight velocity offset of the emission that traces the jet (see the main text). The locus of the line-of-sight component of the velocity of the blueshifted and redshifted jet is indicated with light-blue and red solid lines, respectively. The vertical dashed lines indicate the maximum extent of the CO($J = 2 \rightarrow 1$) emission along PA = 68° and the approximate radius where the outer edge of the H_2O maser clusters are located, respectively. The contours are drawn from 3σ on steps of 3σ ($\sigma = 1$ mJy beam^{-1}).

masers (∼1100 au) is $\approx 50\,\mathrm{km\,s^{-1}}/\sin(\theta_{inc}) = 90\,\mathrm{km\,s^{-1}}$, where $\theta_{inc} = 35°$. The resulting timescale for the shell is $\tau_{shell} \approx 60$ yr.

Thus, the kinematic ages of the jet and the bipolar shell, traced by the continuum emission, are basically equal, strongly suggesting that the former created the latter as it interacted with material in the vicinity of the driving source. The difference in size between the jet and the bipolar shell, despite their common kinematic age, can be explained in the following way. When the highly collimated jet was launched for the first time, around 65 yr ago, it interacted with the dense material close to the central source creating the bipolar shell. As circumstellar material was swept up, the expansion of the bipolar shell slowed down. Additionally, since the jet is launched with a velocity higher than the resulting velocity of the shell, it opens its way out through the shell, creating the physical conditions that favor the H_2O maser emission in the region where the two components interact. Since the edges of the CO($J = 2 \rightarrow 1$) emission are clearly defined and there is no evidence of collimated emission beyond the structures seen in Figure 1, it is likely that W43A is indeed undergoing the earliest phase of collimated mass loss, as suggested previously (Imai et al. 2002). It is worth noting that recent numerical simulations presented by Balick et al. (2020) predict morphologies very similar to that of W43A for certain combinations of initial conditions of the density, velocity, and magnetic field. Therefore, these observational results are of utter importance to constrain such kind of numerical simulations.

3.5. A Binary System in W43A?

The CO($J = 2 \rightarrow 1$) emission associated with the jet also exhibits a clumpy structure. The redshifted jet has nine knots, while the blueshifted jet exhibits only seven knots (see Figure 3). The knots are roughly associated in pairs, although there are some variations in their separations from the central source. The missing knots in the blueshifted jet coincide with the location of one of the continuum bright regions. Thus, it is likely that they are obscured by dense material in the dusty shell. The average knot spacing is 180 au. Similar clumpy structures are commonly found in jets associated with young stellar objects (Hirano et al. 2006, 2010; Lee et al. 2007; Santiago-García et al. 2009) and they are interpreted as due to periodic events of increase of the velocity within the jets (Santiago-García et al. 2009; Hirano et al. 2010). For the case of W43A, this could be explained in terms of a jet-launching mechanism associated with accretion in a binary system that hosts an AGB star and a companion with eccentric orbits. When the components are in periastron the accretion disk is perturbed and the mass-loss rate increases (Bonnell & Bastien 1992; Clarke & Syer 1996; Davis et al. 2013), leading to internal shocks in the jet that produce the observed clumpy structure (Hirano et al. 2006; Santiago-García et al. 2009). Given the knot spacing and the speed of the jet, the time interval between them is around 5–7 yr, which would be equal to the orbital period of the binary system.

4. Final Remarks

The observations presented in this work reveal with unprecedented detail the structure of a highly collimated jet and a bipolar bipolar morphology in the envelope of an AGB star and provide crucial information on the initial conditions of the CSE shaping. Particularly, the physical parameters derived from these observations will be essential to feed the theoretical models and numerical simulations that aim to explain the aspherical morphologies in the late stages of the evolution of low- and intermediate-mass stars

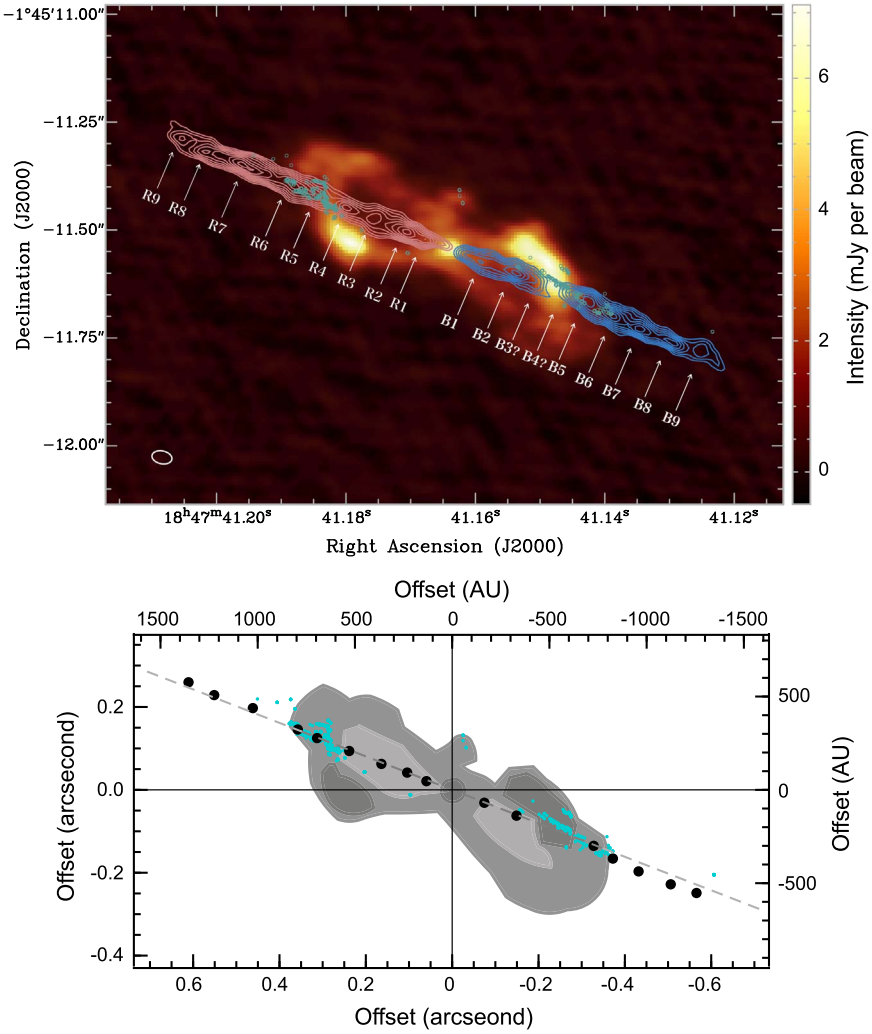

Figure 3. Upper panel: continuum and CO($J = 2 \rightarrow 1$) line emission from W43A. The blue and red contours indicate blueshifted and redshifted CO($J = 2 \rightarrow 1$) emission with velocity offsets >75 km s^{-1}, tracing the jet. The contours are drawn from 3σ on steps of 3σ (σ = 15 mJy km s^{-1}). The color map is the continuum emission at ∼230 GHz. Lower panel: diagram showing the location of the knots of the jet relative to the shell traced by the continuum emission. The origin is the location of the emission peak of the central continuum source: (J2000) R.A. = $18^{h}47^{m}41\overset{s}{.}164$, decl. = $-1°45'11\overset{''}{.}54$. The dashed line indicates a linear fit to the clumps in the inner region of the bipolar lobes. The knots of the blueshifted jet located outside the lobes deviate from the linear fit. In both panels the H_2O masers found during 1994–2007 (Chong et al. 2015) and 2015 are indicated with dots in cyan color (see Appendix E for the details of the H_2O maser observations).

(e.g., Balick et al. 2020 and references therein). Given the short timescale, <100 yr, derived for this transition, it is imperative to investigate the other few (∼15) WF sources (Desmurs 2012) that may exhibit different stages of this ephemeral phase.

This Letter makes use of the following ALMA data: ADS/JAO.ALMA#2016.1.00540.S. ALMA is a partnership of ESO (representing its member states), NSF (USA) and NINS (Japan), together with NRC (Canada), MOST and ASIAA (Taiwan), and KASI (Republic of Korea), in cooperation with the Republic of Chile. The Joint ALMA Observatory is operated by ESO, AUI/NRAO and NAOJ. The VLBA is operated by the National Radio Astronomy Observatory (NRAO) under cooperative agreement by Associated Universities, Inc. J.F.G. is partially supported by MINECO (Spain) grant AYA2017-84390-C2-R (co-funded by FEDER) and by the State Agency for Research of the Spanish MCIU through the "Center of Excellence Severo Ochoa" award for the Instituto de Astrofísica de Andalucía (SEV-2017-0709). H.I. and G.O. are supported by the MEXT KAKENHI program (16H02167). H.I. and J.F.G. were supported by the Invitation Program for Foreign Researchers of the Japan Society for Promotion of Science (JSPS grant S14128). G.O. was supported by the Australian Research Council Discovery project DP180101061 of the Australian government, and the grants of CAS LCWR 2018-XBQNXZ-B-021 and National Key R&D Program 2018YFA0404602 of China. D.T. was supported by the ERC consolidator grant 614264. The authors are grateful to Bruce Balick for careful reading of the Letter and valuable suggestions and comments.

Appendix A
Distance to W43A

In previous works, W43A has been assumed to be located at a distance of $D = 2.6$ kpc from the Sun. This value was calculated assuming the source is in a circular orbit around the Galaxy with an angular velocity given by a Galactic rotation curve derived in the 1960 s (Schmidt 1965; Bowers et al. 1980). In this work, the kinematical distance to W43A is updated using the Revised Kinematic Distance Calculator (2014) using Galactic parameters from model A5 in Reid et al. (2014). The calculator gives near and far kinematical distances of $2.22^{+0.38}_{-0.40}$ kpc and $11.90^{+0.38}_{-0.36}$ kpc,

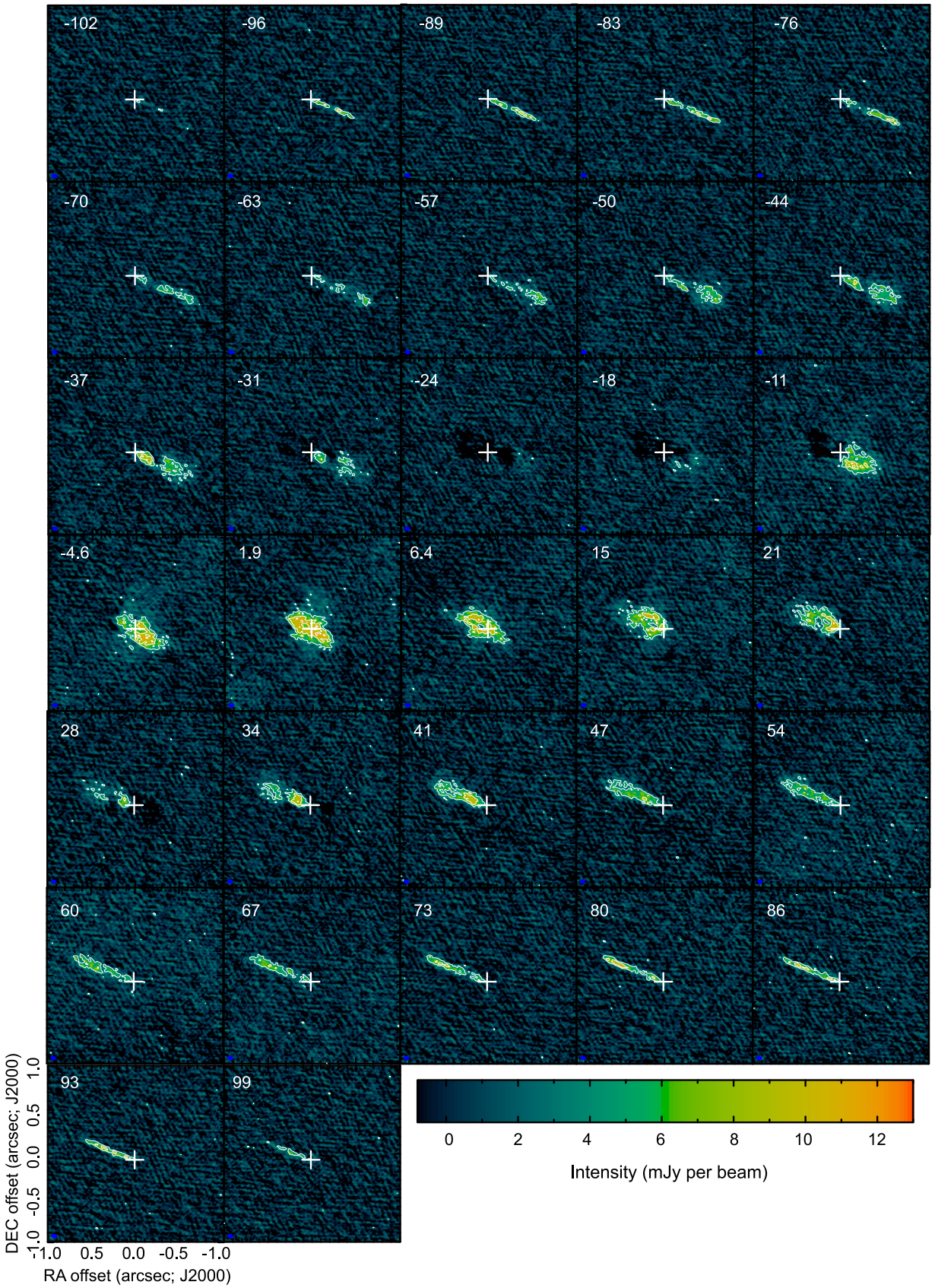

Figure 4. Velocity channel map of the CO($J = 2 \rightarrow 1$) emission from W43A. The contours indicate 5, 10, and 15 times the rms noise level of the maps, 8×10^{-4} Jy beam^{-1}. The numbers in the upper left corner correspond to the velocity offset with respect to the systemic velocity (34 km s^{-1}), $V_{\rm offset}$, of the channel map. The vertical color wedge is in units of Jy beam^{-1}. The white cross is located at the position of the central bright dot that pinpoints the location of the star: (J2000) R.A. = $18^{\rm h}47^{\rm m}41\overset{\rm s}{.}164$, decl. = $-1°45'11\overset{''}{.}54$. The blue ellipse located at the lower left corner indicates the synthesized beam, $\theta_{\rm FWHM} = 0\overset{''}{.}048 \times 0\overset{''}{.}031$, PA = 75°.

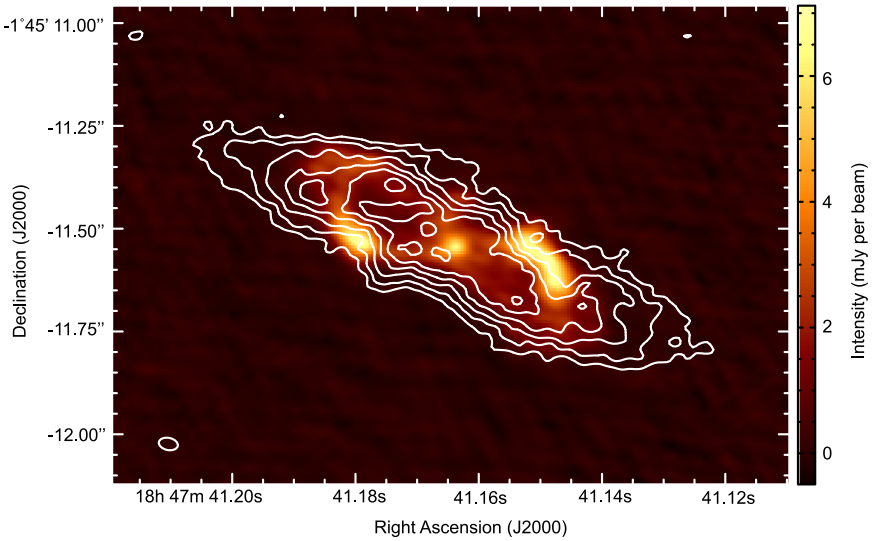

Figure 5. Continuum and p-$H_2S(J_{K_a,K_c} = 2_{20} \rightarrow 2_{11})$ line emission from W43A. The contours represent H_2S emission integrated over the velocity range $-100 < V_{offset}(km\ s^{-1}) < +100$. The contours are (100, 200, 300, 400, 500, 600) mJy beam^{-1} km s^{-1} (σ = 35 mJy beam^{-1} km s^{-1}). The ellipse at the bottom left corner represents the size of the synthesized beam $\theta_{beam} = 0\farcs071 \times 0\farcs048$, PA = 86.°3. The color map is the continuum emission at ~230 GHz.

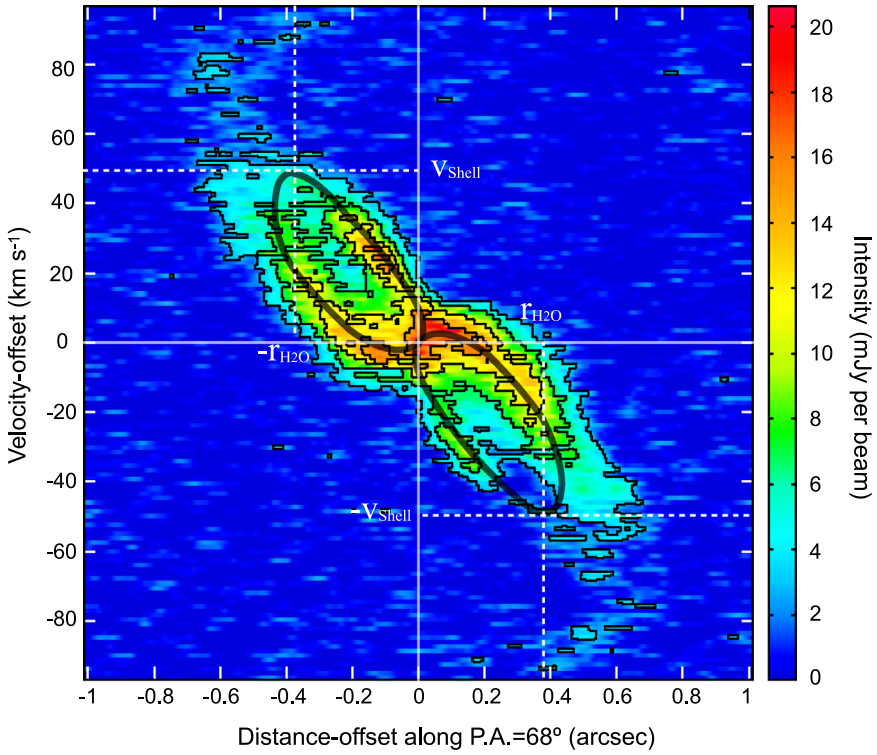

Figure 6. *PV* diagram of the p-$H_2S(J_{K_a,K_c} = 2_{20} \rightarrow 2_{11})$ line emission from W43A. The H_2S emission exhibits the characteristic morphology of a double-lobe structure, indicated with a solid black line, similarly to the shell delineated by the continuum emission. The velocity offset is defined with respect to the systemic velocity of the star V_{sys} = 34 km s^{-1}. The vertical dashed lines indicate the radius where the H_2O masers are located. The horizontal white dashed lines indicate the maximum velocity offset along the line of sight of the shell traced by the p-$H_2S(J_{K_a,K_c} = 2_{20} \rightarrow 2_{11})$ emission. The contours are from 4σ on steps of 4σ (σ = 1 mJy beam^{-1}).

respectively. We adopt the near kinematical distance since it is compatible with the result of the Bayesian Distance Calculator (Reid et al. 2016).

Appendix B
Channel Map of the CO($J = 2 \rightarrow 1$) Emission in W43A

Figure 4 shows a velocity channel map of the CO($J = 2 \rightarrow 1$) emission from W43A.

Appendix C
Velocity-integrated and *PV* Diagram of the H_2S Line Emission in W43A

The contours in Figure 5 represent a velocity-integrated map of the p-$H_2S(J_{K_a,K_c} = 2_{20} \rightarrow 2_{11})$ emission in W43A superimposed on the continuum emission (color map) at ~230 GHz. Figure 6 shows the *PV* diagram of the H_2S emission obtained using a slit along PA = 68°.

Appendix D
Volume Density of the Molecular Gas in the Bipolar Shell

The mass of the gas in the bipolar shell can be estimated assuming optically thin emission and isothermal conditions for the dust. It should be pointed out that although the dust emission is optically thick toward the bright regions, as discussed in the main text, it is reasonable to assume optically thin emission from the rest of the shell. Having this in mind, the mass of the dust can obtained from the following relation (Hildebrand 1983; Gall et al. 2011):

$$M_{\rm d} = \frac{D^2\, S_\nu}{\kappa_\nu B_\nu(T_{\rm d})}, \quad (1)$$

where D is the distance to the source, S_ν is the flux density of the continuum emission, κ_ν is the dust absorption coefficient, and $B_\nu(T_{\rm d})$ is the Planck function evaluated at the temperature of the dust, $T_{\rm d}$. The flux density of the continuum emission that traces the bipolar shell is 267 ± 25 mJy. Considering an average dust temperature $T_{\rm d} = 100$ K, obtained from the brightness temperature of the optically thick bright regions; a dust absorption coefficient $\kappa_\nu = 1.8$ cm^2 g^{-1} for small silicate grains with coating of amorphous carbon (Ossenkopf & Henning 1994); and a dust-to-gas ratio value of 100, the mass of the bipolar shell is 2.0 ± 0.2 solar masses. The volume of the bipolar shell is obtained from the size of the bipolar lobes of molecular gas confined by the shell and from the thickness of the shell. The resulting average density of the bipolar shell is $n_{\rm H_2,Shell} = 5.1 \pm 0.5 \times 10^8$ cm^{-3}. For silicate grains without coating the dust absorption coefficient is $\kappa_\nu \approx 0.15$ cm^2 g^{-1} (Ossenkopf & Henning 1994), resulting in values of the bipolar shell mass and density a factor of 10 larger, which are unrealistically high given that the initial mass of the star must be $M \lesssim 8 M_\odot$.

Appendix E
VLBA Observations of the H_2O Masers

The results of all the VLBA observations presented in this Letter were summarized by Chong et al. (2015). One exception is the one based on the latest observation on 2014 January 19 (project code BI41A). This observation and its data reduction were conducted similarly to those of other observations. The detected H_2O masers include a maser feature located close to the tip of the blueshifted jet, and give the largest extent of the maser distribution. This indicates that the H_2O maser region has grown along the jet at a rate roughly consistent with the proper motions of the individual maser features ($\sim$9 mas yr^{-1} in one side of the bipolar jet). The coordinates of the fringe phase and position reference maser spot at $V_{\rm LSR} = 126.1$ km s^{-1} were determined to be (J2000) R.A. $= 18^{\rm h}47^{\rm m}41\overset{\rm s}{.}1821$, decl. $= -01°45'11\overset{''}{.}396$, with an uncertainty better than 1 mas that may be dominated by the uncertainty in the position of the phase-reference source J183323.9−032331. The superposition of the H_2O maser maps taken from the different observation sessions was made by the spatio-kinematical fitting to the bipolar jet as described by Chong et al. (2015).

ORCID iDs

Daniel Tafoya https://orcid.org/0000-0002-2149-2660
Hiroshi Imai https://orcid.org/0000-0002-0880-0091
José F. Gómez https://orcid.org/0000-0002-7065-542X
Gabor Orosz https://orcid.org/0000-0002-5526-990X

References

Amiri, N., Vlemmings, W., & van Langevelde, H. J. 2010, A&A, 509, A26
Balick, B., Frank, A., & Liu, B. 2020, ApJ, 889, 13
Balick, B., Huarte-Espinosa, M., Frank, A., et al. 2013, ApJ, 772, 20
Bonnell, I., & Bastien, P. 1992, ApJL, 401, L31
Bowers, P. F., Reid, M. J., Johnston, K. J., Spencer, J. H., & Moran, J. M. 1980, ApJ, 242, 1088
Chernin, L., Masson, C., Gouveia dal Pino, E. M., & Benz, W. 1994, ApJ, 426, 204
Chong, S.-N., Imai, H., & Diamond, P. J. 2015, ApJ, 805, 53
Clarke, C. J., & Syer, D. 1996, MNRAS, 278, L23
Davis, P. J., Siess, L., & Deschamps, R. 2013, A&A, 556, A4
Desmurs, J.-F. 2012, in IAU Symp. 287, Cosmic Masers—From OH to H0, ed. R. S. Booth, W. H. T. Vlemmings, & E. M. L. Humphreys (Cambridge: Cambridge Univ. Press), 217
Diamond, P. J., & Nyman, L. Å. 1988, in IAU Symp. 129, The Impact of VLBI on Astrophysics and Geophysics, ed. M. J. Reid & J. M. Moran (Dordrecht: Kluwer Academic), 249
Gall, C., Hjorth, J., & Andersen, A. C. 2011, A&ARv, 19, 43
Herman, J., & Habing, H. J. 1985, A&AS, 59, 523
Hildebrand, R. H. 1983, QJRAS, 24, 267
Hirano, N., Ho, P. P. T., Liu, S.-Y., et al. 2010, ApJ, 717, 58
Hirano, N., Liu, S.-Y., Shang, H., et al. 2006, ApJL, 636, L141
Holdship, J., Viti, S., Jimenez-Serra, I., et al. 2016, MNRAS, 463, 802
Imai, H. 2007, in IAU Symp. 242, Astrophysical Masers and their Environments, ed. J. M. Chapman & W. A. Baan, 279
Imai, H., Nakashima, J.-i., Diamond, P. J., Miyazaki, A., & Deguchi, S. 2005, ApJL, 622, L125
Imai, H., Obara, K., Diamond, P. J., Omodaka, T., & Sasao, T. 2002, Natur, 417, 829
Lagadec, E., Verhoelst, T., Mékarnia, D., et al. 2011, MNRAS, 417, 32
Lee, C.-F., Ho, P. T. P., Hirano, N., et al. 2007, ApJ, 659, 499
Likkel, L., & Morris, M. 1988, ApJ, 329, 914
Ossenkopf, V., & Henning, T. 1994, A&A, 291, 943
Reid, M. J., Dame, T. M., Menten, K. M., & Brunthaler, A. 2016, ApJ, 823, 77
Reid, M. J., Menten, K. M., Brunthaler, A., et al. 2014, ApJ, 783, 130
Sahai, R., Morris, M. R., & Villar, G. G. 2011, AJ, 141, 134
Sahai, R., & Trauger, J. T. 1998, AJ, 116, 1357
Santiago-García, J., Tafalla, M., Johnstone, D., & Bachiller, R. 2009, A&A, 495, 169
Schmidt, M. 1965, Rotation Parameters and Distribution of Mass in the Galaxy (Chicago, IL: Univ. Chicago Press), 513
Tafoya, D., Orosz, G., Vlemmings, W. H. T., Sahai, R., & Pérez-Sánchez, A. F. 2019, A&A, 629, A8
Vlemmings, W. H. T., Diamond, P. J., & Imai, H. 2006, Natur, 440, 58
Wilson, W. J., & Barrett, A. H. 1972, A&A, 17, 385
Yates, J. A., Field, D., & Gray, M. D. 1997, MNRAS, 285, 303